Crystal Structure and Site-Directed Mutagenesis Analyses of Haloalkane Dehalogenase LinB from *Sphingobium* sp. Strain MI1205

Masahiko Okai,[a] Jun Ohtsuka,[a] Lica Fabiana Imai,[a] Tomoko Mase,[a] Ryota Moriuchi,[b] Masataka Tsuda,[b] Koji Nagata,[a] Yuji Nagata,[b] Masaru Tanokura[a]

Department of Applied Biological Chemistry, Graduate School of Agricultural and Life Sciences, University of Tokyo, Tokyo, Japan[a]; Department of Environmental Life Sciences, Graduate School of Life Sciences, Tohoku University, Sendai, Japan[b]

The enzymes LinB$_{UT}$ and LinB$_{MI}$ (LinB from *Sphingobium japonicum* UT26 and *Sphingobium* sp. MI1205, respectively) catalyze the hydrolytic dechlorination of β-hexachlorocyclohexane (β-HCH) and yield different products, 2,3,4,5,6-pentachlorocyclohexanol (PCHL) and 2,3,5,6-tetrachlorocyclohexane-1,4-diol (TCDL), respectively, despite their 98% identity in amino acid sequence. To reveal the structural basis of their different enzymatic properties, we performed site-directed mutagenesis and X-ray crystallographic studies of LinB$_{MI}$ and its seven point mutants. The mutation analysis revealed that the seven amino acid residues uniquely found in LinB$_{MI}$ were categorized into three groups based on the efficiency of the first-step (from β-HCH to PCHL) and second-step (from PCHL to TCDL) conversions. Crystal structure analyses of wild-type LinB$_{MI}$ and its seven point mutants indicated how each mutated residue contributed to the first- and second-step conversions by LinB$_{MI}$. The dynamics simulation analyses of wild-type LinB$_{MI}$ and LinB$_{UT}$ revealed that the entrance of the substrate access tunnel of LinB$_{UT}$ was more flexible than that of LinB$_{MI}$, which could lead to the different efficiencies of dehalogenation activity between these dehalogenases.

Hexachlorocyclohexane (HCH) is a six-chlorine-substituted cyclohexane. One of its isomers, the γ isomer, has insecticidal properties and has been widely used as an insecticide around the world (1). Although the use of γ-HCH has been prohibited in most countries due to its toxicity and long persistence, the large-scale production, widespread use, and dumping of the other non-insecticidal isomers (α-, β-, and δ-HCHs) in past decades still continue to create problems with HCH contamination in soil and groundwater (2). β-HCH in particular is a persistent and problematic isomer of HCH.

Several β-HCH-degrading bacteria whose β-HCH-degrading enzymes can be utilized for bioremediation have been identified (3–5). LinB$_{MI}$ and LinB$_{UT}$ are haloalkane dehalogenases isolated from *Sphingobium* sp. MI1205 and *Sphingobium japonicum* UT26, respectively, that can cleave the carbon-halogen bond in β-HCH. Haloalkane dehalogenases belong to the α/β-hydrolase family, and their catalytic mechanism consists of the following steps: (i) substrate binding, (ii) cleavage of the carbon-halogen bond in the substrate and formation of an intermediate covalently bound to the nucleophile, (iii) hydrolysis of the alkyl-enzyme intermediate, and (iv) release of halide ion and alcohol (6). LinB$_{MI}$ and LinB$_{UT}$ share 98% sequence identity, with only 7 different amino acid residues (at positions 81, 112, 134, 135, 138, 247, and 253) out of 296 residues, but these enzymes exhibit different enzymatic properties (Fig. 1). LinB$_{MI}$ catalyzes the two-step dehalogenation and converts β-HCH to 2,3,4,5,6-pentachlorocyclohexanol (PCHL) and further to 2,3,5,6-tetrachlorocyclohexane-1,4-diol (TCDL) (7) in the manner of LinB2 from *Sphingomonas* sp. BHC-A (8) and LinB from *Sphingobium indicum* B90A (9), whereas LinB$_{UT}$ catalyzes only the first-step dehalogenation of β-HCH to PCHL (10) and cannot degrade PCHL further. Moreover, LinB$_{MI}$ can catalyze the first-step conversion eight times as efficiently as LinB$_{UT}$ (7).

In a previous site-directed mutagenesis study, the V134I, H247A, and V134I H247A mutants of LinB$_{MI}$, in which one or two LinB$_{MI}$-specific residues were mutated to a LinB$_{UT}$-type resi-

due(s), showed reduced activities in both the first- and second-step dehalogenations, with the exception that there was no reduction in the first-step dehalogenation activity of the H247A mutant (7). However, the activities of these mutants were still higher than that of LinB$_{UT}$ in both the first- and second-step dehalogenations, which suggested that one or more of the other five residues (T81, V112, T135, L138, and I253) uniquely found in LinB$_{MI}$ were also important for the high dehalogenation activity of LinB$_{MI}$. To date, the crystal structure of LinB$_{UT}$ has been described (11–14), whereas the crystal structure of LinB$_{MI}$ has not. To investigate how the seven residues that are different between LinB$_{MI}$ and LinB$_{UT}$ contribute to their different enzymatic properties, we performed site-directed mutagenesis and X-ray crystallographic studies of LinB$_{MI}$ and its seven point mutants, where each LinB$_{MI}$-specific residue is mutated to the LinB$_{UT}$-type residue (T81A, V112A, V134I, T135A, L138I, H247A, and I253M). Activity measurements were made for all the mutants except for those carrying the V134I and H247A mutations, whose measurements were reported previously (7).

MATERIALS AND METHODS

Expression, purification, and crystallization. The expression plasmids of wild-type LinB$_{MI}$ and the seven mutants (carrying T81A, V112A, V134I, T135A, L138I, H247A, and I253M) were constructed using the vector pAQNM, where the target proteins were expressed under the control of the *tac* promoter and *lacI*^{q} (7). Wild-type LinB$_{MI}$ and the seven mutants were expressed and purified by the following procedures. *Escherichia coli*

A

B

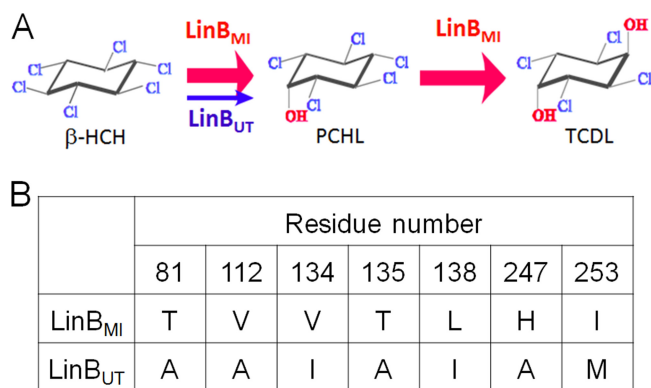|	Residue number						
	81	112	134	135	138	247	253
LinB$_{MI}$	T	V	V	T	L	H	I
LinB$_{UT}$	A	A	I	A	I	A	M

FIG 1 Different enzymatic properties between LinB$_{MI}$ and LinB$_{UT}$. (A) β-HCH degradation reactions catalyzed by LinB$_{MI}$ and LinB$_{UT}$. LinB$_{MI}$ converts β-HCH to PCHL and further to TCDL, while LinB$_{UT}$ catalyzes only the first-step conversion of β-HCH to PCHL. The activity of LinB$_{MI}$ is approximately eight times as high as that of LinB$_{UT}$ in the first-step dehalogenation of β-HCH to PCHL (7). (B) The seven amino acid residues that are different between LinB$_{MI}$ and LinB$_{UT}$.

strain BL21(DE3) cells (Novagen) were cultured in Luria-Bertani (LB) medium containing 50 μg ml^{-1} ampicillin until an optical density at 600 nm (OD$_{600}$) of 0.6 at 37°C. Protein expression was induced by adding isopropyl β-D-thiogalactopyranoside (IPTG) to a final concentration of 1 mM, and the culture was continued at 25°C for 12 h. The cells were harvested by centrifugation at 4,500 × g at 4°C for 10 min. The harvested cells were suspended in Sol A (50 mM Tris-HCl [pH 7.5], 400 mM NaCl, and 5 mM imidazole) and disrupted by sonication. After centrifugation at 40,000 × g for 30 min at 4°C, the supernatant was loaded onto a 3-ml Ni Sepharose 6 Fast Flow column (GE Healthcare) at room temperature. After a wash step with Sol B (50 mM Tris-HCl [pH 7.5], 400 mM NaCl, and 50 mM imidazole), the protein was eluted with Sol C (50 mM Tris-HCl [pH 7.5], 400 mM NaCl, and 200 mM imidazole). The purified protein was dialyzed against 20 mM Tris-HCl (pH 8.0) and then concentrated to 25 mg ml^{-1} using a Vivaspin 20 concentrator (Sartorius) at 4°C.

Initial crystallization trials of LinB$_{MI}$ were performed by the sitting-drop vapor diffusion method in 96-well Intelli-Plate plates (Art Robbins Instruments) using Crystal Screen HT, Index HT (Hampton Research), and Wizard I and II (Emerald Biosystems) sparse-matrix screening kits. Each drop was prepared by mixing equal volumes (0.7 μl) of the protein solution and a reservoir solution and equilibrated against 70 μl of the reservoir solution at 4°C or 20°C. Further crystallization trials were carried out based on the crystallization conditions of the untagged (100 mM Tris-HCl [pH 8.8 to 9.0], 200 mM CaCl$_2$, and 17 to 19% [wt/vol] polyethylene glycol [PEG] 6000) and His-tagged (100 mM Tris-HCl [pH 8.5], 200 mM MgCl$_2$. and 20% [wt/vol] PEG 4000) LinB$_{UT}$ by the sitting-drop vapor diffusion method in 24-well plates (Hampton Research) (14, 15). The crystallization drops were prepared by mixing 1.0 μl protein solution and 1.0 μl reservoir solution and were equilibrated against 0.3 ml reservoir solution.

Data collection and processing. The crystals of wild-type LinB$_{MI}$ and the seven mutants were transferred to the reservoir solution containing 25% (vol/vol) glycerol as the cryoprotectant. The X-ray diffraction data were collected at a wavelength of 1.0000 Å in a cryogenic nitrogen gas stream at beamlines BL-5A and AR-NW12A of the Photon Factory (Ibaraki, Japan). The data sets were obtained by collecting 360 frames, with an oscillation step of 0.5°. The diffraction data were indexed, integrated, and scaled using the HKL-2000 software package (16).

Structure modeling and refinement. The crystal structure of wild-type LinB$_{MI}$ was determined by the molecular replacement method using the software program MOLREP (17) and the crystal structure of LinB$_{UT}$ (PDB code 1CV2) (11) as the initial model. Refinements were performed

using the Coot (18) and Refmac5 (19) programs. Water molecules were added using ARP/wARP software (20). Then, the crystal structures of the seven mutants were solved by molecular replacement using the wild-type structure of LinB$_{MI}$ as the initial model. The stereochemical quality of each final model was assessed using the Ramachandran plots obtained by the RAMPAGE software program (21).

Molecular dynamics simulation. The atomic coordinates of the crystal structures of wild-type LinB$_{MI}$ (PDB code 4H77), solved in this study, and LinB$_{UT}$ (PDB code 1CV2) (11) were used as the initial models. The following dynamics simulations were performed using the software program MOE2011.10 with the default parameter settings unless otherwise stated. The missing hydrogen atoms of wild-type LinB$_{MI}$ and LinB$_{UT}$ were generated and energy minimized using the MMFF94x (Merck molecular force field 94x) force field with distance-dependent dielectric electrostatics. Then, a few potassium ions for neutralization and explicit water molecules were added within a sphere of 10 Å from the protein surfaces. The resulting protein and solvent molecules in the spherical droplet were energy minimized using the MMFF94x force field with R-field electrostatics. Tether weight was applied to all nonhydrogen atoms during the energy minimization steps. The molecular-dynamics simulations were performed using the NVT ensemble and the Nosé-Poincaré-Anderson (NPA) algorithm at 303 K with a time step of 1 fs and without any bond constraint. As for the first 100-ps dynamics, the tether weight was applied to all nonhydrogen atoms and gradually reduced. After the first 100-ps dynamics, the dynamics simulations were performed for 14 ns without any positional restraint. The atomic coordinates were recorded every 1 ps after the first 100-ps dynamics and used for trajectory analysis.

Ligand-docking simulation. The ligand-docking simulations were performed using the ASEDock software program, a docking program based on a shape similarity assessment between a concave portion on a protein and a ligand, in the Molecular Operating Environment (MOE) software package (Chemical Computing Group, Montreal, Canada). The three-dimensional structures of β-HCH and PCHL were modeled using the Molecule Builder in MOE. The initial models were energy minimized, employing the MMFF94x force field. The active site of the LinB structure was detected using the Alpha Site Finder in MOE. For each ligand, 250 conformations were generated using the default LowModeMD search parameters. The scoring function used by ASEDock was based on the protein-ligand interaction energies. The interaction energy (U_{dock}) of a given conformation was calculated as the sum of U_{ele} (electric energy), U_{vdw} (van der Waals energy), and U_{strain} (difference of the minimal energies between the docked ligand and the ligand which was located nearest the docked ligand).

Enzymatic assays. For enzymatic assays, *E. coli* BL21 Star(DE3) cells (Invitrogen) expressing LinB and its mutants were disrupted by bacteriolysis using a CelLytic B reagent (Sigma), and His-tagged enzymes were purified by using BD Talon metal affinity resins (BD Biosciences). The purified enzymes were incubated with 17 μM β-HCH in 50 mM potassium phosphate buffer (pH 7.5) containing 10% (vol/vol) glycerol at 30°C. The enzyme concentration in the reaction mixture was 150 μg/ml. The mixture (100 μl) was extracted with an equal volume of ethyl acetate and then analyzed using a Shimadzu GC-17A gas chromatograph with an ^{63}Ni electron capture detector (ECD) and Rtx-1 capillary column (30 m by 0.25 μm by 0.25 μm; Restek). The column temperature was increased from 160°C to 200°C at a rate of 4°C/min for the separation of the peak of PCHL from that of TCDL and then from 200°C to 260°C at a rate of 20°C/min. The gas flow rate was 30 ml/min. As the internal standard, 10 μM 2,4,5-trichlorophenol was used. Kinetic data were fitted to the irreversible two-step reaction structure of HCH conversion to TCDL via PCHL (Scheme 1) by using the GEPASI 3.2 software program (22). The specificity constants and their standard errors for both reaction steps (k_1 and k_2) were obtained from the calculation. Evolutionary programming (23) was used to optimize the kinetic constants during the fitting of the kinetic data to Scheme 1. Values given are the means of triplicates. Due to
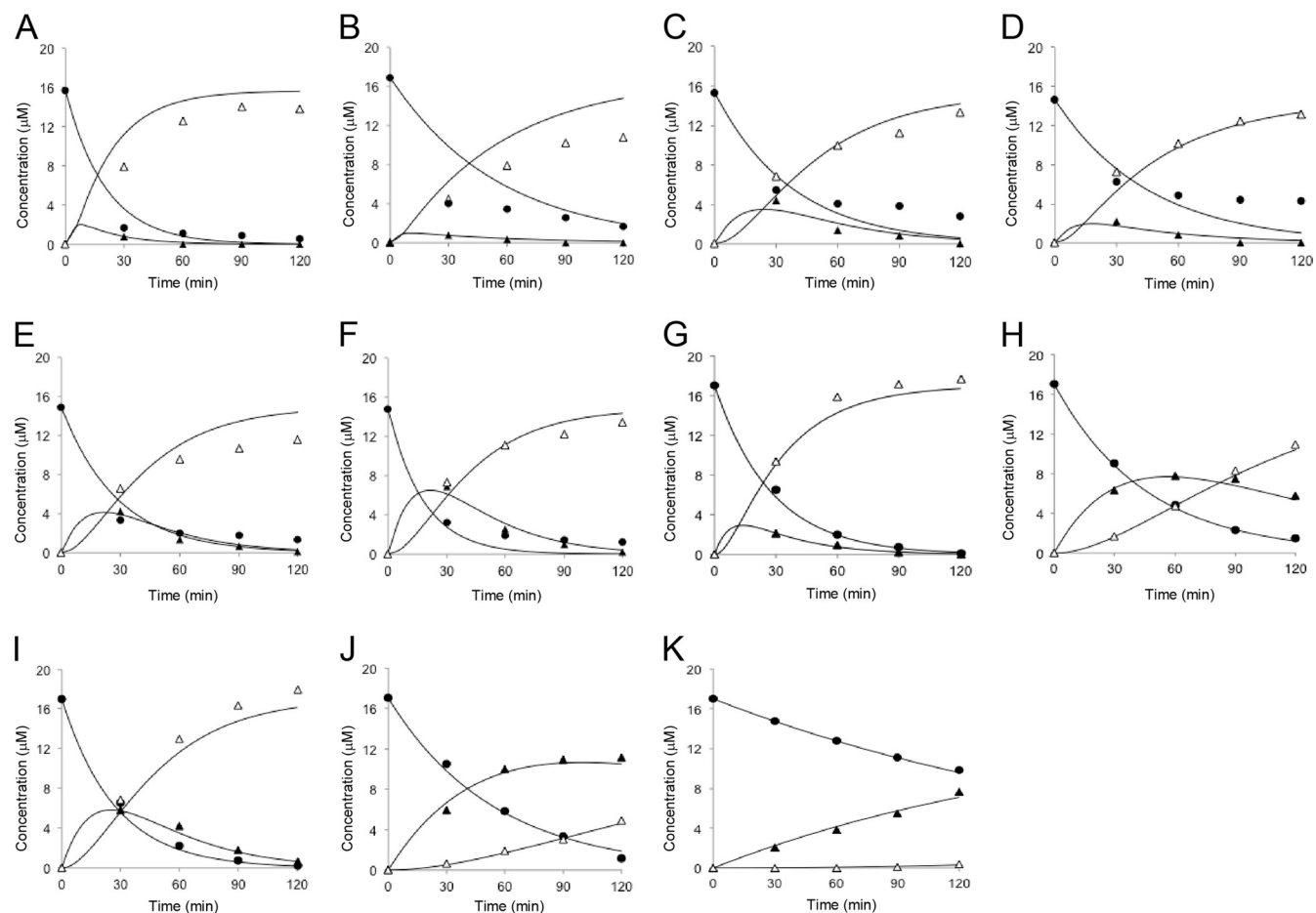
FIG 2 Degradation of β-HCH (black circles) and appearance of its metabolites, PCHL (black triangle) and TCDL (white triangle), in reaction mixtures containing $LinB_{MI}$ wild type (A), $LinB_{MI}$ T81A (B), $LinB_{MI}$ V112A (C), $LinB_{MI}$ T135A (D), $LinB_{MI}$ L138I (E), $LinB_{MI}$ I253M (F), $LinB_{MI}$ wild type (G), $LinB_{MI}$ V134I (H), $LinB_{MI}$ H247A (I), $LinB_{MI}$ V134I/H247A (J), or $LinB_{UT}$ wild type (K). The same data (G to K) used in reference 7 are also shown in this study. The activity data (A to F) of this study were obtained by the same research group as for reference 7 under the same reaction conditions except for the concentration of purified enzyme (100 and 150 μg/ml in the work described in reference 7 and this study, respectively).

the low solubility (17 μM) of β-HCH in water, the k_{cat} and K_m values of these mutants could not be calculated.

$$E + HCH \xrightarrow{k_1} E + PCHL \xrightarrow{k_2} E + TCDL$$
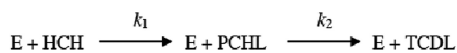
Scheme 1

Protein structure accession numbers. The atomic coordinates and structure factors (PDB codes 4H77, 4H7D, 4H7E, 4H7F, 4H7H, 4H7I, 4H7J and 4H7K) have been deposited in the Protein Data Bank.

RESULTS AND DISCUSSION

Site-directed mutagenesis. The wild-type $LinB_{MI}$ enzyme used in reference 7 and this study gave comparable data with the same research group, as shown in Fig. 2A and G. We examined the dehalogenation activities of the point mutants of $LinB_{MI}$, in which each of the five residues (T81, V112, T135, L138, and I253) was mutated to the corresponding residue in $LinB_{UT}$ (Table 1 and Fig. 2B to F). The V112A (Fig. 2C), T135A (Fig. 2D), and L138I (Fig. 2E) mutants showed reduced activities in both the first- and second-step dehalogenations. The I253M (Fig. 2F) mutant retained full activity in the first-step dehalogenation but showed reduced activity in the second-step dehalogenation as in the case of the H247A (Fig. 2I) mutant (7). On the other hand, the T81A (Fig. 2B)

mutant showed reduced activity in the first-step dehalogenation but retained full activity in the second-step dehalogenation. Our mutational data combined with the previous data reported by Ito et al. (7) revealed that one (T81), two (H247 and I253), and four

TABLE 1 Specificity constants of wild-type $LinB_{MI}$ and its mutants

Enzyme	Specificity constant, k_{cat}/K_m ($mM^{-1} s^{-1}$)	
	HCH → PCHL	PCHL → TCDL
$LinB_{MI}$ wild type	0.19 ± 0.008	1.0 ± 0.3
$LinB_{MI}$ T81A	0.070 ± 0.003	0.95 ± 0.5
$LinB_{MI}$ V112A	0.10 ± 0.009	0.23 ± 0.04
$LinB_{MI}$ T135A	0.080 ± 0.005	0.42 ± 0.1
$LinB_{MI}$ L138I	0.13 ± 0.01	0.22 ± 0.04
$LinB_{MI}$ I253 M	0.21 ± 0.03	0.14 ± 0.02
$LinB_{MI}$ wild type[a]	0.205 ± 0.005	0.716 ± 0.052
$LinB_{MI}$ V134I[a]	0.124 ± 0.005	0.080 ± 0.003
$LinB_{MI}$ H247A[a]	0.210 ± 0.015	0.240 ± 0.021
$LinB_{MI}$ V134I H247A[a]	0.104 ± 0.003	0.027 ± 0.001
$LinB_{UT}$[b]	0.0271 ± 0.0002	0.0036 ± 0.0006

[a] The same data used in reference 7 are shown.
[b] $LinB_{UT}$ is identical to $LinB_{MI}$ T81A V112A V134I T135A L138I H247A I253M.

TABLE 2 Data collection and refinement statistics for wild-type LinB$_{MI}$ and the seven mutants

Statistic		Value for LinB$_{MI}$ with mutation (PDB code)							
		None (4H77)	T81A (4H7D)	V112A (4H7E)	V134I (4H7F)	T135A (4H7H)	L138I (4H7I)	H247A (4H7J)	I253M (4H7K)
Diffraction data collection									
Beamline		Photon Factory AR-NW12A	Photon Factory BL-5A	Photon Factory BL-5A	Photon Factory BL-5A	Photon Factory AR-NW12A	Photon Factory BL-5A	Photon Factory BL-5A	Photon Factory AR-NW12A
Detector		ADSC Quantum 210	ADSC Quantum 210	ADSC Quantum 210	ADSC Quantum 315r	ADSC Quantum 210	ADSC Quantum 315r	ADSC Quantum 210	ADSC Quantum 210
Wavelength (Å)		1.0000	1.0000	1.0000	1.0000	1.0000	1.0000	1.0000	1.0000
Space group		$P2_12_12$	$P2_12_12$	$P2_12_12$	$P2_12_12$	$P2_12_12$	$P2_12_12$	$P2_12_12$	$P2_12_12$
Unit-cell parameters (Å)	$a = $	50.4	50.4	50.4	50.5	50.4	50.4	50.4	50.5
	$b = $	72.1	72.1	72.2	72.3	71.7	72.3	72.2	72.2
	$c = $	73.5	73.5	73.9	73.6	73.1	73.9	73.2	73.6
Resolution (Å)[a]		20–1.60 (1.66–1.60)	20–1.95 (1.98–1.95)	20–1.80 (1.86–1.80)	20–1.80 (1.86–1.80)	20–2.10 (2.14–2.10)	20–1.80 (1.86–1.80)	20–1.80 (1.83–1.80)	20–1.75 (1.78–1.75)
No. of measurements		258,109	125,465	174,986	165,876	92,137	176,684	167,404	190,853
No. of unique reflections		36,060	19,954	25,428	25,649	16,096	25,640	24,924	27,832
Completeness (%)[a]		99.9 (99.9)	99.2 (91.7)	100.0 (100.0)	99.8 (98.7)	99.9 (99.6)	99.8 (98.2)	97.3 (97.7)	99.8 (98.2)
R_{sym}[a,b]		0.068 (0.314)	0.087 (0.279)	0.101 (0.339)	0.084 (0.283)	0.110 (0.397)	0.075 (0.270)	0.071 (0.194)	0.093 (0.367)
$<I>/<\sigma(I)>$[a]		32.0 (5.3)	37.7 (9.3)	31.1 (6.1)	39.0 (7.9)	23.7 (4.6)	30.5 (5.6)	41.7 (9.4)	37.3 (5.3)
Refinement									
Resolution range (Å)		20–1.60	20–1.95	20–1.80	20–1.80	20–2.10	20–1.80	20–1.80	20–1.75
R_{work} (%)[c]		15.9	17.7	17.4	17.7	18.6	17.2	17.5	17.2
R_{free} (%)[d]		19.1	21.0	19.8	20.0	25.0	19.3	19.6	20.5
RMSD									
Bonds (Å)		0.010	0.008	0.007	0.007	0.009	0.007	0.006	0.007
Angles (°)		1.371	1.310	1.160	1.253	1.371	1.230	1.220	1.298
Ramachandran plot									
Favored region (%)		96.6	96.9	96.9	96.9	96.2	96.6	96.9	96.2
Allowed region (%)		3.4	3.1	3.1	3.1	3.8	3.4	3.1	3.8
Outlier region (%)		0.3	0	0	0	0	0	0	0

[a] Values in parentheses are for the highest-resolution shell.
[b] $R_{sym} = \Sigma_{hkl}\,\Sigma_i\,|I_i(hkl) - <I(hkl)>|/\Sigma_{hkl}\,\Sigma_i\,I_i(hkl)$, where $<I(hkl)>$ is the average intensity of symmetry relation reflections.
[c] $R_{work} = \Sigma_{hkl}||F_{obs}| - |F_{calc}||/\Sigma_{hkl}|F_{obs}|$.
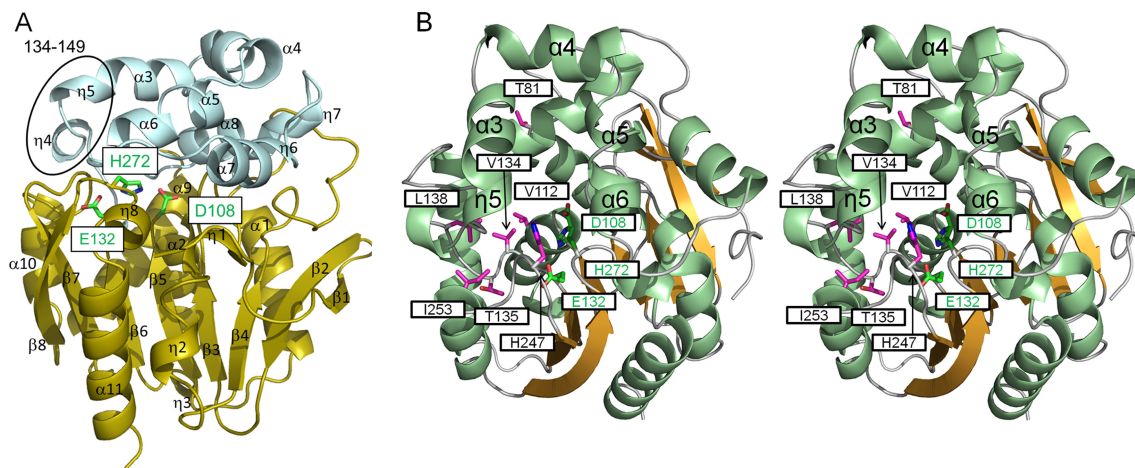[d] R_{free} was calculated by using the 5% of reflections excluded in the refinement.

FIG 3 Structure of wild-type LinB$_{MI}$. (A) Ribbon diagram of wild-type LinB$_{MI}$. The core domain (residues 2 to 132 and 214 to 295) and the cap domain (residues 133 to 213) are colored olive and light blue, respectively. The catalytic triad residues are shown as stick models. The most flexible region (residues 134 to 149) in LinB$_{MI}$ is circled in black. (B) Stereo view of wild-type LinB$_{MI}$. The helices and strands are colored light green and orange, respectively. The catalytic triad residues and the residues which are different from the corresponding residues in LinB$_{UT}$ are shown as stick models and colored green and magenta, respectively.

(V112, V134, T135, and L138) of the seven different residues between LinB$_{MI}$ and LinB$_{UT}$ contributed to their different efficiencies in the first step, the second step, and both steps of dehalogenation, respectively.

Crystallization and data collection. We obtained LinB$_{MI}$ crystals by combining the reported crystallization conditions for untagged and His-tagged LinB$_{UT}$ (14, 15). The best crystals, with typical dimensions of 0.2 by 0.4 by 0.01 mm, were obtained by mixing 1.0 μl of the protein solution (25 mg ml^{-1}) and 1.0 μl of the reservoir solution (100 mM Tris-HCl (pH 8.0), 20% (wt/vol) PEG 4000, and 200 mM CaCl$_2$) at 5°C. Similarly, the crystals of the seven mutants of LinB$_{MI}$ were obtained by mixing 1.0 μl of the protein solution (25 mg ml^{-1}) and 1.0 μl of the reservoir solution (100 mM Tris-HCl (pH 7.8 to 8.1), 17 to 20% (wt/vol) PEG 4000, and 200 mM CaCl$_2$) at 5°C.

The crystal of wild-type LinB$_{MI}$ belonged to the space group $P2_12_12$ with the following unit cell dimensions: $a = 50.4$ Å, $b = 72.1$ Å, and $c = 73.5$ Å. It contained one LinB$_{MI}$ molecule per asymmetric unit. The Matthews coefficient (24) and the solvent content were 1.96 Å^3 Da^{-1} and 37%, respectively. The crystals of the seven mutants had the same space group, $P2_12_12$, with unit cell dimensions similar to those of the crystal of wild-type LinB$_{MI}$. The diffraction data statistics for these crystals are given in Table 2.

Overall structures of the wild type and seven mutants of LinB$_{MI}$. We have solved the crystal structures of wild-type LinB$_{MI}$ at a 1.60-Å resolution and of the seven mutants at 1.75- to 2.10-Å resolutions by molecular replacement. The LinB$_{MI}$ molecule existed as a monomer in the crystal and consisted of two domains, the core domain and the cap domain (Fig. 3A). The core domain (residues 2 to 132 and 214 to 295) had a typical α/β-hydrolase fold, as seen in other haloalkane dehalogenases (25–29). Unlike the core domain, the cap domain varied in the number and orientations of helices among haloalkane dehalogenases, and the cap domain (residues 133 to 213) of LinB$_{MI}$ was composed of four 3$_{10}$ and six α-helices. The crystal structures of the wild type and the seven mutants of LinB$_{MI}$ were very similar to one another, with root mean square deviations (RMSDs) for C^α atoms (residues 2 to 295) of 0.095 to 0.31 Å.

In LinB$_{MI}$, D108, H272, and E132 formed the catalytic triad as in LinB$_{UT}$ (Fig. 3A). D108, located on the β5 strand, acted as the nucleophile. The O^{δ2} atom of D108 formed a hydrogen bond with the N^ε atom of H272, which was located on the loop between the β8 strand and the η8 helix. The N^δ atom of H272 formed a hydrogen bond with the O^{ε1} atom of E132, which was located on the β6 strand.

The reservoir solution used contained 200 mM CaCl$_2$, and the electron density of one calcium ion was clearly observed between two adjacent LinB$_{MI}$ molecules aligned in the crystal. The calcium ion was coordinated with the O^{δ1} and O^{δ2} atoms in the side chain of D166 in a LinB$_{MI}$ molecule, the main chain O atoms of P175 and I178 of an adjacent LinB$_{MI}$ molecule, and three water molecules. Thus, the calcium ion plays an important role for the growth of this crystal by mediating the above intermolecular interaction.

The electron density of one chloride ion was observed in the active site, and the chloride ion formed hydrogen bonds with two halide-stabilizing residues, N38 and W109. These hydrogen bonds would reflect the manner of recognition of a chloride ion released from the substrate.

Effects of different residues located near the active site on the specificity constants. The residue at position 134 was the nearest residue to the nucleophile residue D108 among the seven residues that are different between LinB$_{MI}$ and LinB$_{UT}$ (Fig. 3B) and is likely to bind the substrate directly. The V134I mutant of LinB$_{MI}$ retained 60% of the first-step dehalogenation activity but showed only 11% of the second-step dehalogenation activity compared with those of wild-type LinB$_{MI}$ (7). The superimposition of the crystal structures of wild-type LinB$_{MI}$ and the V134I mutant revealed that the presence or absence of the C^δ atom at position 134 was the only difference around the active site between these two structures (Fig. 4A). To understand the effect of the C^δ atom at position 134, we performed cocrystallization and soaking experiments using β-HCH but could not obtain the crystal structure of LinB$_{MI}$ complexed with β-HCH. Then, we predicted the locations and orientations of β-HCH and PCHL when bound to wild-type LinB$_{MI}$ and the V134I mutant using the ASEDock program of MOE. The docking simulation provided reasonable binding mod-
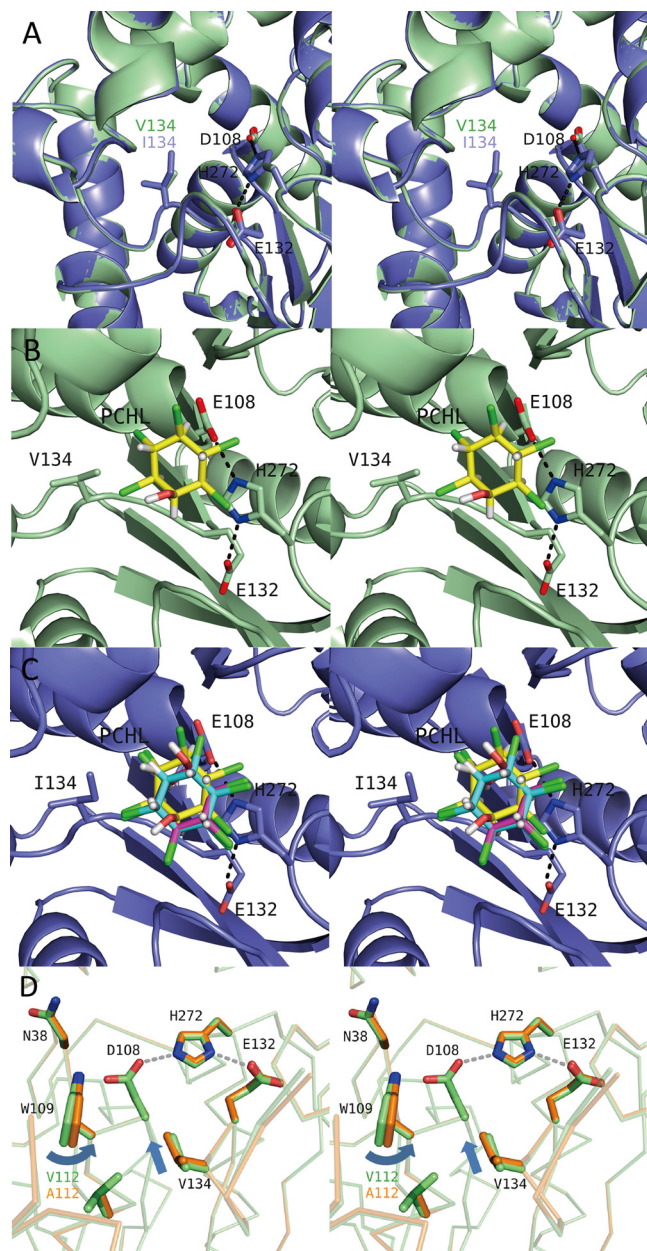
FIG 4 Different amino acid residues located around the active site between LinB$_{MI}$ and LinB$_{UT}$. (A) Superimposition of the active sites of the wild type (light green) and the V134I mutant (slate) of LinB$_{MI}$. The catalytic triad residues (D108, E132, and H272) and V134/I134 are labeled. (B and C) Docking simulations of the wild type (B) or the V134I mutant (C) with PCHL. The chlorine, oxygen, and hydrogen atoms of the PCHL molecules are colored green, red, and white, respectively. In wild-type LinB$_{MI}$, the PCHL model with the lowest binding energy is shown, and its carbon atoms are colored yellow. In the V134I mutant, the carbon atoms are colored cyan, magenta, and yellow in the PCHL models with the lowest binding, the second-lowest binding and the highest interaction energies, respectively. (D) Superimposition of the active sites between the wild type (light green) and the V112A mutant (orange).

els of β-HCH for both wild-type LinB$_{MI}$ and the V134I mutant. The β-HCH molecules docked in wild-type LinB$_{MI}$ and the V134I mutant were located at the same position with almost the same orientations (data not shown). On the other hand, the docking simulation with PCHL gave different results for wild-type LinB$_{MI}$

and the V134I mutant. In the top three solutions, the interaction energies of the PCHL molecule with wild-type LinB$_{MI}$ were −1.6, 1.8, and 3.4 kcal/mol, and those with the V134I mutant were −14.7, −1.1, and 2.3 kcal/mol. In wild-type LinB$_{MI}$, the manner of binding of PCHL in the top solution could explain the occurrence of the second-step conversion from PCHL to TCDL, with the distance between the O^{δ2} atom of D108 and the C-4 atom of PCHL being 3.1 Å (Fig. 4B). However, in the case of the V134I mutant, the positions and orientations of the bound PCHL models in the top two solutions (Fig. 4C, cyan and magenta) were different from those in the top solution for wild-type LinB$_{MI}$. The C-4 atoms in the two PCHL models were 4.7 Å away from the O^{δ2} atom of D108, and thus the second-step conversion from PCHL to TCDL was unlikely to occur. The binding manner of the third solution (Fig. 4C, yellow) for the V134I mutant was almost the same as that in the top solution for wild-type LinB$_{MI}$. These docking simulation results suggested that the V134I mutant of LinB$_{MI}$ was not likely to bind PCHL properly for the second-step conversion to occur because of the presence of the C^{δ} atom at position 134.

The residue at position 112 was located at the bottom of the substrate binding pocket (Fig. 3B). The V112A mutant of LinB$_{MI}$ retained 53% of the first-step dehalogenation activity but showed only 23% of the second-step dehalogenation activity of wild-type LinB$_{MI}$ (7). In the V112A mutant, the main chain of V134 was shifted by 0.3 Å toward the catalytic residue (D108) compared with the corresponding region in wild-type LinB$_{MI}$, and the side chain of W109, one of the two halide-stabilizing residues, was rotated 6° relative to that in wild-type LinB$_{MI}$ around the C^{γ}-C^{δ1} bond (Fig. 4D). Such structural differences at the two residues should be due to the absence of the C^{γ2} atom rather than the C^{γ1} atom in the V112A mutant of LinB$_{MI}$. These structural changes within the active-site pocket should cause a reduction in first- and second-step dehalogenation activities in the V112A mutant of LinB$_{MI}$.

Effects of different residues lining the substrate access tunnel on specificity constants. The active site of LinB$_{MI}$ was buried deeply inside the enzyme. Three entrances to the substrate access tunnels were found in LinB$_{MI}$ using the software program CAVER (Fig. 5A). Two tunnel entrances (Fig. 5A, purple and cyan) were formed by the η5, α3, α5, and α6 helices, and the other tunnel entrance (Fig. 5A, pink) was formed by the two helices (η4 and α10) and a loop between the β7 strand and the α10 helix. A tunnel entrance (Fig. 5B, purple) found in LinB$_{UT}$, which was formed by the α6 helix and two loops between the η4 and η5 helices and between the β7 strand and the α10 helix, was not observed in LinB$_{MI}$ because the side chain of His247 covered the entrance. Ito et al. reported that H247 in LinB$_{MI}$ was important for the second-step conversion of PCHL to TCDL (7). In the H247A mutant structure, the η5 helix was shifted toward the α6 helix because the H247A mutation created an extra space, which resulted in conformational changes of the side chains of F143 and P144 (Fig. 5C). Thus, the side chain of H247 would contribute to the tunnel formation suitable for substrate (PCHL) entry and product (TCDL) release.

L138 and I253 of LinB$_{MI}$ were involved in the formation of one access tunnel (Fig. 5A, pink), while T135 was located approximately 6 Å away from the tunnel. The orientations of the side chain at position 253 were divided into two groups among the wild type and mutants of LinB$_{MI}$. In wild-type LinB$_{MI}$ and the
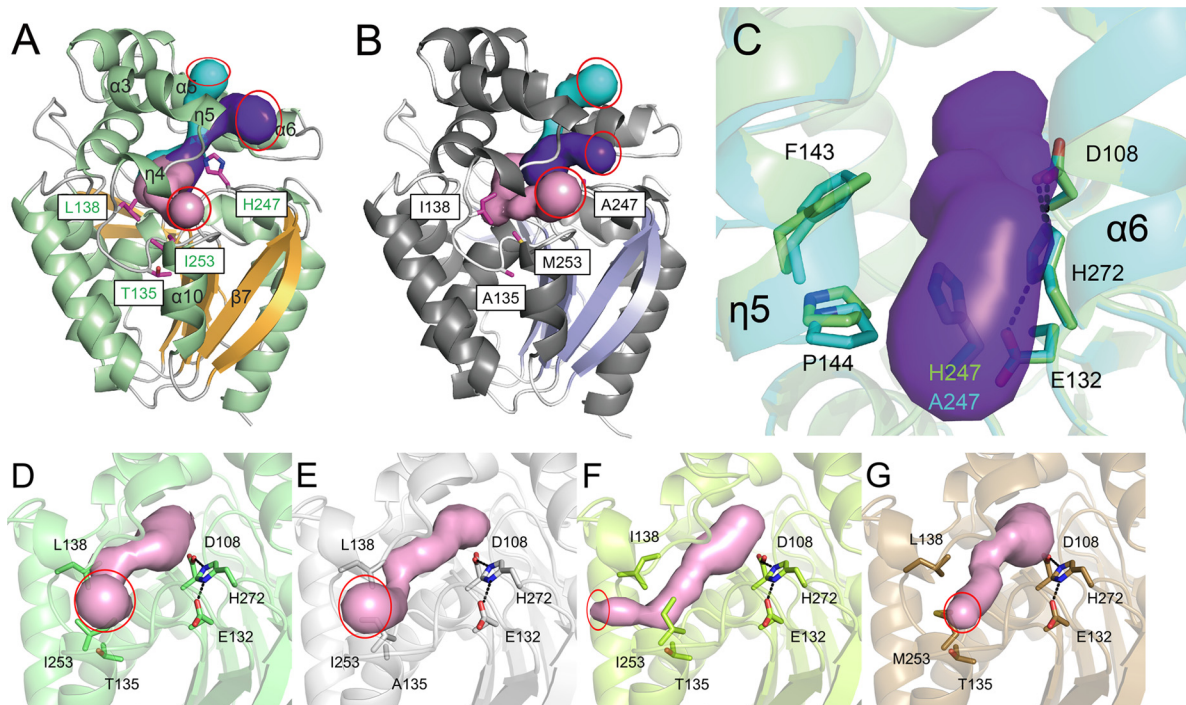
FIG 5 Different amino acid residues lining the access tunnel between LinB$_{MI}$ and LinB$_{UT}$. (A and B) The three access tunnels (pink, purple, and cyan) to the active site of wild-type LinB$_{MI}$ (A) or LinB$_{UT}$ (B). The catalytic triad residues (green) and amino acid residues (magenta) that are different between wild-type LinB$_{MI}$ and LinB$_{UT}$ are shown as stick models. The red circles represent the entrances of the access tunnels. (C) Superimposition between the wild type (light green) and the H247A mutant (cyan) of LinB$_{MI}$. The tunnel (purple) observed in wild-type LinB$_{MI}$ is shown. The catalytic triad residues and the residues at positions 135, 138, and 253 are shown as sticks in the wild-type (D), T135A mutant (E), L138I mutant (F), or I253M mutant (G) structure of LinB$_{MI}$. The red circles show the entrances of the access tunnels of the wild type and three mutants.

T81A, V112A, V134I, and H247A mutants, the C$^\beta$-C$^{\gamma 1}$-C$^{\delta 1}$ chain of I253 faced toward the side chain of T135 (Fig. 5D). In contrast, in the T135A and L138I mutants, the C$^\beta$-C$^{\gamma 1}$-C$^{\delta 1}$ chains of I253 faced toward the side chain of L138 (Fig. 5E and F). Thus, the T135A and L138I mutations caused the conformational changes of the side chain of I253, which resulted in the changes of the size and position of a tunnel entrance (Fig. 5D to F). In the I253M mutant (Fig. 5G), the side chain of M253 faced toward the side chain of L138, and the side chain of L138 was rotated approximately 90° relative to that in wild-type LinB$_{MI}$ along the C$^\beta$-C$^\gamma$

bond. In contrast, in LinB$_{UT}$, the side chain of M253 faced toward the side chain of A135 (Fig. 6) (11). Thus, the orientation of the side chain of M253 could be influenced by the residues at position(s) 135 and/or 138. Since the residue at position 253 was located at an entrance of the access tunnel, the irregular orientation of the side chain at position 253 affected the shape of the entrance of the access tunnel in the T135A, L138I, and I253M mutants (Fig. 5E to G). The irregular forms of the tunnel entrances in these mutants should lead to the reductions in the dehalogenase activities, especially the second-step dehalogenation activity.
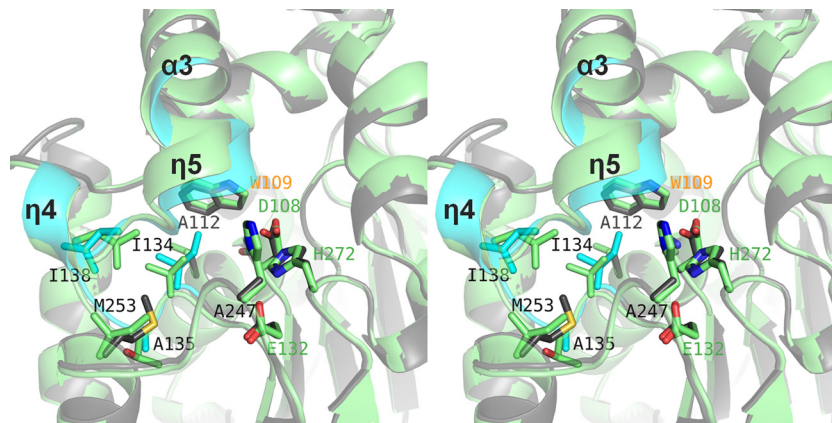

FIG 6 Structural comparison between wild-type LinB$_{MI}$ and LinB$_{UT}$. Superimposition between wild-type LinB$_{MI}$ (light green) and LinB$_{UT}$ (cyan and dark gray) is shown. The most noteworthy difference between wild-type LinB$_{MI}$ and LinB$_{UT}$ is colored cyan in LinB$_{UT}$. The catalytic triad residues, one (W109) of two halide-stabilizing residues, and six of the residues that are different between wild-type LinB$_{MI}$ and LinB$_{MI}$ are shown as stick models and labeled.
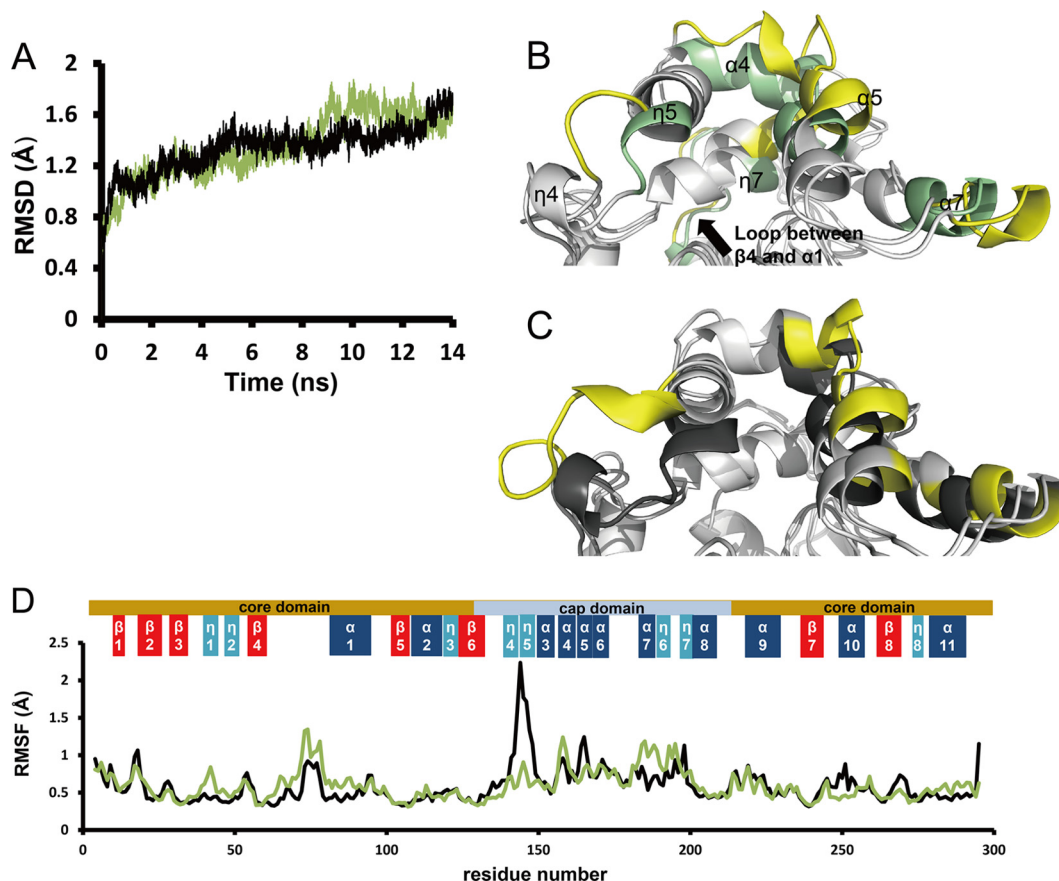
FIG 7 Molecular dynamics (MD) simulations of wild-type $LinB_{MI}$ and $LinB_{UT}$. (A) Time course of C^{α} RMSDs from the initial structures of wild-type $LinB_{MI}$ (green) and $LinB_{UT}$ (black) during MD simulations. (B) Superposition of the crystal structure (gray and green) and the structure after the simulation (gray and yellow) of wild-type $LinB_{MI}$. (C) Superposition of the crystal structure (gray and black) and the structure after the simulation (gray and yellow) of wild-type $LinB_{UT}$. Green, black, and yellow in panels B and C indicate the most different regions observed between the crystal structures and the structures after the simulations (gray and yellow). (D) C^{α} RMSFs for $LinB_{MI}$ (green) and $LinB_{UT}$ (black) residues over the last 2-ns simulations.

In wild-type $LinB_{MI}$, T81 was positioned outside the active site, and the side chain of T81 formed hydrogen bonds with one water molecule and the amide nitrogen of E84. The main-chain structure of the T81A mutant was very similar to that of wild-type $LinB_{MI}$, with an RMSD of 0.12 Å, and no conformational change was observed either at the active site or in the access tunnel between wild-type $LinB_{MI}$ and the T81A mutant.

Structural comparison between $LinB_{MI}$ and $LinB_{UT}$. $LinB_{MI}$ and $LinB_{UT}$ share 98% sequence identity. Their overall structures were very similar to each other, with an RMSD of 0.27 Å for 292 C^{α} atoms. The most remarkable structural difference between $LinB_{MI}$ and $LinB_{UT}$ was observed at the N-terminal region of the cap domain (residues 134 to 149) (Fig. 3A and 6), which plays an important role in determining the shape and size of the active site and the substrate access tunnels. A structural difference similar to that between $LinB_{MI}$ and $LinB_{UT}$ was observed between wild-type $LinB_{MI}$ and the H247A mutant (Fig. 5C). The main chain of I134 in $LinB_{UT}$ was shifted by 0.8 Å toward the catalytic residue (D108) compared with that in $LinB_{MI}$, and the side chain of W109 in $LinB_{UT}$ was rotated approximately 5° relative to that in $LinB_{MI}$ (Fig. 6). These structural differences would be due to the size of the amino acid residue at position 112 (Val in $LinB_{MI}$ versus Ala in $LinB_{UT}$), considering the structural difference between wild-type $LinB_{MI}$ and the V112A mutant.

We performed molecular dynamics simulations to reveal the molecular mechanisms of the different efficiencies in dehalogenation between $LinB_{MI}$ and $LinB_{UT}$. In both the cases of $LinB_{MI}$ and $LinB_{UT}$, the C^{α} RMSDs against the initial coordinates increased sharply in the first nanosecond of the simulations, and the RMSDs were in the range of 1.4 to 1.8 Å in the last two nanoseconds (12 to 14 ns) (Fig. 7A), indicating that no global conformational change occurred. Figures 7B and C show the superpositions of the crystal structures and the structures after the simulation of $LinB_{MI}$ and $LinB_{UT}$, respectively. In the core domain of $LinB_{UT}$, the crystal and the simulated structures were almost identical. In contrast, in the core domain of $LinB_{MI}$, a conformational change was observed in a loop (residues 76 to 81) between the β4 strand and the α1 helix, which would be due to T81, the only residue in this region unique to $LinB_{MI}$. The conformational change in the loop could lead to a movement of the interacting η7 helix in the cap domain toward the α4 helix and a concomitant change in the shape of the substrate binding pocket, which might cause the different efficiencies in first-step dehalogenation activities between two enzymes. As for the cap domain, similar conformational changes were observed in both $LinB_{MI}$ and $LinB_{UT}$ in the following regions: η4-(loop)-η5, α4, α5, and α7. The conformational change at the entrance of the substrate access tunnel from the η4 to η5 helices in $LinB_{UT}$ was larger than that in $LinB_{MI}$, allowing the substrates to

enter the tunnel easily (Fig. 7B and C). The different residues at positions 247 and 253 should cause the different conformational changes in this region. Root mean square fluctuation (RMSF) was used as an index of structural flexibility. The RMSF analysis (Fig. 7D) clearly shows that the entrance of the substrate access tunnel from the η4 to η5 helices (residues 142 to 146) of LinB$_{UT}$ is much more flexible than that of LinB$_{MI}$. This high flexibility in LinB$_{UT}$ would lead to the large conformational change at the entrance of the substrate access tunnel, as shown in Fig. 7B. In DhaA, a member of the same α/β-hydrolase family as LinB, the molecular dynamics simulation analysis revealed that the narrower substrate access tunnel in a variant than in the wild-type enzyme shielded the active site from the solvent and showed higher activity than that of the wild-type enzyme (30). Similarly, the low flexibility of the tunnel entrance in LinB$_{MI}$ would contribute to the increase in its dehalogenation activity by inhibiting the influx of water molecules into the active site, particularly for second-step dehalogenation activity, where the water molecules can compete with the hydroxyl group of PCHL.

Concluding remarks. We have analyzed the dehalogenation activities of five of the seven amino acid residues that differ between LinB$_{MI}$ and LinB$_{UT}$. This and previous mutagenesis analyses revealed that most of the seven residues had effects on second-step dehalogenation and none of the seven residues were critical for degradation activity. We have determined the crystal structures of the wild type and the seven mutants of LinB$_{MI}$. The structural comparisons among wild-type LinB$_{MI}$, LinB$_{UT}$, and the seven mutants of LinB$_{MI}$ indicated that each mutant except the T81A mutant caused a small conformational change in the access tunnels or the active site that resulted in a reduction in the first- and second-step dehalogenation activities of LinB$_{UT}$ compared with those of LinB$_{MI}$. The dynamics simulations of wild-type LinB$_{MI}$ and LinB$_{UT}$ suggested that the flexibility of the entrance of the substrate access tunnel led to the difference in dehalogenation activity, peculiarly the second-step activity.

ACKNOWLEDGMENTS

REFERENCES

1. **Willett KL, Ulrich EM, Hites RA.** 1998. Differential toxicity and environmental fates of hexachlorocyclohexane isomers. Environ. Sci. Technol. **32:**2197–2207.

2. **Walker K, Vallero DA, Lewis RG.** 1999. Factors influencing the distribution of lindane and other hexachlorocyclohexanes in the environment. Environ. Sci. Technol. **33:**4373–4378.

3. **Johri AK, Dua M, Tuteja D, Saxena R, Saxena DM, Lal R.** 1998. Degradation of α, β, γ and δ-hexachlorocyclohexanes by *Sphingomonas paucimobilis*. Biotechnol. Lett. **20:**885–887.

4. **Gupta A, Kaushik CP, Kaushik A.** 2000. Degradation of hexachlorocyclohexane (HCH; α, β, γ and δ) by *Bacillus circulans* and *Bacillus brevis* isolated from soil contaminated with HCH. Soil Biol. Biochem. **32:**1803–1805.

5. **Gupta A, Kaushik CP, Kaushik A.** 2001. Degradation of hexachlorocyclohexane isomers by two strains of *Alcaligenes faecalis* isolated from a contaminated site. Bull. Environ. Contam. Toxicol. **66:**794–800.

6. **Prokop Z, Monincová M, Chaloupková R, Klvaňa M, Nagata Y, Janssen DB, Damborský J.** 2003. Catalytic mechanism of the haloalkane dehalogenase LinB from *Sphingomonas paucimobilis* UT26. J. Biol. Chem. **278:**45094–45100.

7. **Ito M, Prokop Z, Klvaňa M, Otsubo Y, Tsuda M, Damborský J, Nagata Y.** 2007. Degradation of β-hexachlorocyclohexane by haloalkane dehalogenase LinB from γ-hexachlorocyclohexane-utilizing bacterium *Sphingobium* sp. MI1205. Arch. Microbiol. **188:**313–325.

8. **Wu J, Hong Q, Han P, He J, Li S.** 2007. A gene *linB2* responsible for the conversion of β-HCH and 2,3,4,5,6-pentachlorocyclohexanol in *Sphingomonas* sp. BHC-A. Appl. Microbiol. Biotechnol. **73:**1097–1105.

9. **Sharma P, Raina V, Kumari R, Malhotra S, Dogra C, Kumari H, Kohler HP, Buser HR, Holliger C, Lal R.** 2006. Haloalkane dehalogenase LinB is responsible for β- and δ-hexachlorocyclohexane transformation in *Sphingobium indicum* B90A. Appl. Environ. Microbiol. **72:**5720–5727.

10. **Nagata Y, Prokop Z, Sato Y, Jerabek P, Kumar A, Ohtsubo Y, Tsuda M, Damborský J.** 2005. Degradation of β-hexachlorocyclohexane by haloalkane dehalogenase LinB from *Sphingomonas paucimobilis* UT26. Appl. Environ. Microbiol. **71:**2183–2185.

11. **Marek J, Vévodová J, Smatanová IK, Nagata Y, Svensson LA, Newman J, Takagi M, Damborský J.** 2000. Crystal structure of the haloalkane dehalogenase from *Sphingomonas paucimobilis* UT26. Biochemistry **39:**14082–14086.

12. **Oakley AJ, Prokop Z, Boháč M, Kmuniček J, Jedlička T, Monincová M, Kuta-Smatanová I, Nagata Y, Damborský J, Wilce MC.** 2002. Exploring the structure and activity of haloalkane dehalogenase from *Sphingomonas paucimobilis* UT26: evidence for product- and water-mediated inhibition. Biochemistry **41:**4847–4855.

13. **Streltsov VA, Prokop Z, Damborský J, Nagata Y, Oakley A, Wilce MC.** 2003. Haloalkane dehalogenase LinB from *Sphingomonas paucimobilis* UT26: X-ray crystallographic studies of dehalogenation of brominated substrates. Biochemistry **42:**10104–10112.

14. **Oakley AJ, Klvaňa M, Otyepka M, Nagata Y, Wilce MC, Damborský J.** 2004. Crystal structure of haloalkane dehalogenase LinB from *Sphingomonas paucimobilis* UT26 at 0.95 Å resolution: dynamics of catalytic residues. Biochemistry **43:**870–878.

15. **Smatanová I, Nagata Y, Svensson LA, Takagi M, Marek J.** 1999. Crystallization and preliminary X-ray diffraction analysis of haloalkane dehalogenase LinB from *Sphingomonas paucimobilis* UT26. Acta Crystallogr. D **55:**1231–1233.

16. **Otwinowski Z, Minor W.** 1997. Processing of X-ray diffraction data collected in oscillation mode. Methods Enzymol. **276:**307–326.

17. **Vagin A, Teplyakov A.** 1997. MOLREP: an automated program for molecular replacement. J. Appl. Crystallogr. **30:**1022–1025.

18. **Emsley P, Cowtan K.** 2004. Coot: model-building tools for molecular graphics. Acta Crystallogr. D **60:**2126–2132.

19. **Murshudov GN, Vagin AA, Dodson EJ.** 1997. Refinement of macromolecular structures by the maximum-likelihood method. Acta Crystallogr. D **53:**240–255.

20. **Perrakis A, Morris R, Lamzin VS.** 1999. Automated protein model building combined with iterative structure refinement. Nat. Struct. Biol. **6:**458–463.

21. **Lovell SC, Davis IW, Arendall WB, III, de Bakker PI, Word JM, Prisant MG, Richardson JS, Richardson DC.** 2003. Structure validation by Cα geometry: Φ,Ψ and Cβ deviation. Proteins **50:**437–450.

22. **Mendes P.** 1997. Biochemistry by numbers: simulation of biochemical pathways with Gepasi 3. Trends Biochem. Sci. **22:**361–363.

23. **Baeck T, Fogel DB, Michalewicz Z.** 1997. Handbook of evolutionary computation. IOP Publishing/Oxford University Press, Oxford, United Kingdom.

24. **Matthews BW.** 1968. Solvent content of protein crystals. J. Mol. Biol. **33:**491–497.

25. **Verschueren KH, Franken SM, Rozeboom HJ, Kalk KH, Dijkstra BW.** 1993. Refined X-ray structures of haloalkane dehalogenase at pH 6.2 and pH 8.2 and implications for the reaction mechanism. J. Mol. Biol. **232:**856–872.

26. **Newman J, Peat TS, Richard R, Kan L, Swanson PE, Affholter JA, Holmes IH, Schindler JF, Unkefer CJ, Terwilliger TC.** 1999. Haloalkane dehalogenases: structure of a *Rhodococcus* enzyme. Biochemistry **38:**16105–16114.

27. **Pavlová M, Klvaňa M, Jesenská A, Prokop Z, Konečná H, Sato T, Tsuda M, Nagata Y, Damborský J.** 2007. The identification of catalytic pentad in

the haloalkane dehalogenase DhmA from *Mycobacterium avium* N85: reaction mechanism and molecular evolution. J. Struct. Biol. **157**:384–392.

28. **Mazumdar PA, Hulecki JC, Cherney MM, Garen CR, James MN.** 2008. X-ray crystal structure of *Mycobacterium tuberculosis* haloalkane dehalogenase Rv2579. Biochim. Biophys. Acta **1784**:351–362.

29. **Hesseler M, Bogdanović X, Hidalgo A, Berenguer J, Palm GJ, Hinrichs W, Bornscheuer UT.** 2011. Cloning, functional expression, biochemical characterization, and structural analysis of a haloalkane dehalogenase from *Plesiocystis pacifica* SIR-1. Appl. Microbiol. Biotechnol. **91**:1049–1060.

30. **Pavlová M, Klvaňa M, Prokop Z, Chaloupková R, Banás P, Otyepka M, Wade RC, Tsuda M, Nagata Y, Damborský J.** 2009. Redesigning dehalogenase access tunnels as a strategy for degrading an anthropogenic substrate. Nat. Chem. Biol. **5**:727–733.